PNAS RESEARCH ARTICLE | APPLIED PHYSICAL SCIENCES

Mechanistic framework for reduced-order models in soft materials: Application to three-dimensional granular intrusion

Shashank Agarwal[a], Daniel I. Goldman[b], and Ken Kamrin[a,1]

Edited by David Weitz, Harvard University, Cambridge, MA; received August 15, 2022; accepted December 4, 2022

Soft materials often display complex behaviors that transition through apparent solid- and fluid-like regimes. While a growing number of microscale simulation methods exist for these materials, reduced-order models that encapsulate the macroscale physics are often desired to predict how external bodies interact with soft media. Such an approach could provide direct insights in diverse situations from impact and penetration problems to locomotion over natural terrains. This work proposes a systematic program to develop three-dimensional (3D) reduced-order models for soft materials from a fundamental basis using continuum symmetries and rheological principles. In particular, we derive a reduced-order, 3D resistive force theory (3D-RFT), which is capable of accurately and quickly predicting the resistive stress distribution on arbitrary-shaped bodies intruding through granular media. Aided by a continuum description of the granular medium, a comprehensive set of spatial symmetry constraints, and a limited amount of reference data, we develop a self-consistent and accurate 3D-RFT. We verify the model capabilities in a wide range of cases and show that it can be quickly recalibrated to different media and intruder surface types. The premises leading to 3D-RFT anticipate application to other soft materials with strongly hyperlocalized intrusion behavior.

soft matter | intrusion modeling | resistive force theory | continuum modeling | granular media

Significance

This work proposes a general theory for modeling diverse granular intrusion problems such as animal and human locomotion in sands and other natural terrains. Respecting numerous physical constraints, the theory allows for modeling arbitrary motion of three-dimensional generally shaped objects in granular media in near real-time. Moreover, the work provides a generic mechanistic framework for developing self-consistent physics-informed reduced-order models for a wider class of soft materials.

Intrusion in soft media is a common occurrence in nature arising in biological and vehicular locomotion, excavation and anchoring applications, and meteorite and ballistic impact problems (1–4). Modeling intrusion in real-time is critical for a variety of applications and would enable heuristic understanding and quick insight into phenomena like biological circumnutation (5) and robot-terrain interactions (6). But the multiphase nature of these materials—simultaneous solid- and fluid-like behaviors (7)—makes modeling such systems computationally challenging. In the specific case of dry granular media, despite over a century of progress in the disciplines of granular physics and terramechanics—the study of the interaction of tracked vehicles on various substrates (8)—challenges remain. Many commonly used methods have limited applicability due to their shape- or media-specific nature. For instance, commonly used terramechanical empirical models such as the Bekker model (9), later modified by Wong and Reece (10), and the "Magic formulae" (11) are limited to specific geometries such as circular wheels. Inspired by an analogous approach for viscous fluids (12, 13), in recent years, a granular resistive force theory (RFT) has been introduced (14) to model the forces on arbitrarily shaped intruders in granular media, but its form is limited to two-dimensional (2D) problems. This poses limits on its usage in many practical applications. Attempts to extend RFT to three-dimensional (3D) intruders have only recently been explored based on empirical fitting, though these approaches have known limitations (5, 15) (see *SI Appendix*, section S1 for comparison and critique).

While granular intrusions represent a wide class of intrusion problems, equally plentiful problems exist in other soft material systems such as muds and slurries. The challenges are further exacerbated by the 3D nature of such problems that require additional physical self-consistency constraints. Thus, this work introduces a generic program for developing intrusion models in a wide class of soft materials and exemplifies its use in the case of dry granular media. The basic program is to combine three ingredients from the full-field physics of the soft media to extract a "hyperlocalized" rule-set for determining intrusive stresses. First, a continuum model that parsimoniously represents the rheology of the media is identified. Second, dimensional analysis of the continuum system together with surface-media boundary stress constraints are used to obtain a generic functional form for the local intrusion stress formula. Third, global symmetries are enforced to reduce the remaining functional dependences. In our application to

Author affiliations: [a]Department of Mechanical Engineering, Massachusetts Institute of Technology, Cambridge 02139; and [b]Department of Physics, Georgia Institute of Technology, Atlanta 30332

Author contributions: S.A., D.I.G., and K.K. designed research; S.A. performed research; S.A. and K.K. analyzed data; D.I.G. provided comments on the narrative and modified the manuscript; and S.A. and K.K. wrote the paper.

The authors declare no competing interest.

This article is a PNAS Direct Submission.

[1]To whom correspondence may be addressed. Email: kkamrin@mit.edu.

This article contains supporting information online at http://www.pnas.org/lookup/suppl/doi:10.1073/pnas.2214017120/-/DCSupplemental.

Published January 17, 2023.

dry granular intrusions herein, the final step is to fill in the remaining details of the resulting functions using a targeted set of in silico reference tests. We use this program to develop a 3D-RFT model with additional efforts to keep its structure similar to the previous 2D-RFT. We test the 3D-RFT model against a variety of granular intrusions, consisting of the arbitrary motion of many symmetric and asymmetric shapes in beds of granular media. We find excellent agreement between the reference results and 3D-RFT predictions both globally (total intrusion force and moment) and locally (surface stress distribution). Thus, the proposed set of steps, which could also be extended to other soft flowable materials, helps us develop a 3D-RFT framework that satisfies all needed physical constraints, is robust and predictive, and whose dependence on material parameters and surface roughness is transparent. We further discuss the approach's use in material systems other than noncohesive granular media in the *Conclusion* and *SI Appendix*, section S2.

1. Review of Existing RFT

The resistive force theory methodology was originally introduced by Gray and Hancock (12) for modeling self-propelling undulatory biological systems in viscous fluids. In this model, a simple approximate formula for the resistive force on a segment of a thin body is derived from the Stokes equations as a function of the segment's velocity components, orientation, and a few variables characterizing the fluid-segment interaction. Importantly, the theory assumes decoupling of the forces over the various segments of the body (13). The success of fluid RFT motivated multiple studies (14, 16, 17) to explore the existence of a similar theory in granular media.

Li et al. (14) proposed a planar (or 2D) version of RFT for dry granular media (2D-RFT). In 2D-RFT, at low-speeds, the rate-independent nature of granular media (characterized by low values of the nondimensional (micro-) inertial number I (18–20) and macroinertial number I_{mac}, *Materials and Methods*) makes the intrusion force independent of the velocity magnitude. Assuming that material strength increases with pressure and that pressure is primarily due to gravity, Li's 2D-RFT model has the following form:

$$\boldsymbol{F}^{\mathrm{total}} = \int_{\mathrm{surf}} (\alpha_x(\beta,\gamma), \alpha_z(\beta,\gamma))\, |z|\, ds. \qquad [1]$$

Here, $\boldsymbol{F}^{\mathrm{total}}$ represents the total force on an intruding surface, which is divided into smaller planar subsurface elements of area ds and depth $|z|$ from the free surface. The tilt angle β and angle of attack γ characterize the orientation and motion of each surface element of the intruding body (Fig. 1*A*). The vector-valued function of angles $\boldsymbol{\alpha} = (\alpha_x, \alpha_z)$ represents the force per unit area per unit depth; this function must be obtained a priori through experiments or simulations of plate drag and depends on the material properties of the granular media, the intruder surface interaction, and the value of gravity. Of note, Eq. **1** assumes no correlation between the forces on different subsurfaces; only details local to a surface element determine the force on that element (16). A comprehensive comparison of various existing reduced-order methods for modeling granular intrusions, including 2D-RFT and a terramechanical model, can be referred from Agarwal et al. (2).

In recent years, it has been shown that plasticity-based PDE models can also obtain the form of 2D granular RFT (21). More recently, the performance of the continuum approach in modeling a variety of granular intrusions has been demonstrated for wheeled locomotion, impact and penetration, and multibody intrusion (2, 22–25). Additionally, the approach also provides insight into the somewhat-surprising observation that granular RFT is often more accurate than its viscous fluid counterpart (12, 13). Thus, while experimental observations primarily drove the original RFT discoveries, the availability of faster computational methods, the success of 2D-RFT, and a need for better real-time 3D granular intrusion methods have driven the exploration of 3D-RFT. Our work combines the capabilities of the continuum approach with a few symmetry requirements and DEM data to accurately and efficiently model the physics of 3D granular intrusion to develop a 3D-RFT based on our proposed mechanistic framework. We briefly discuss the details of the continuum approach next.

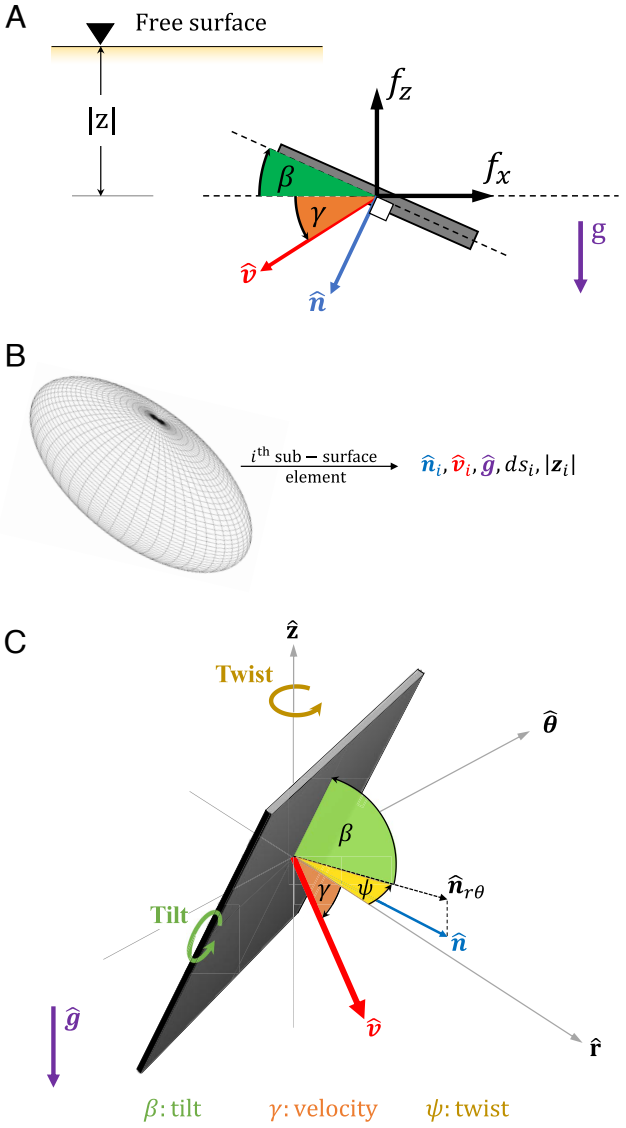

Fig. 1. 2D and 3D RFT surface characterization—2D-RFT: (*A*) Any moving subsurface (line element) is represented using a set of two characteristic angles—plate tilt (β, green) and angle of attack (γ, orange). 3D-RFT: (*B*) Any moving subsurface (plate element) is represented using surface normal ($\hat{\boldsymbol{n}}$) and velocity direction ($\hat{\boldsymbol{v}}$). The force is given from these directions together with the area magnitude (ds), depth ($|z|$), and gravity direction ($\hat{\boldsymbol{g}}$). (*C*) Directions $\hat{\boldsymbol{n}}$ and $\hat{\boldsymbol{v}}$ are expressed using three characteristic angles—plate tilt (β, green), plate twist (ψ, yellow), and velocity angle (γ, orange) in the local coordinate frame $\{\hat{\boldsymbol{r}}, \hat{\boldsymbol{\theta}}, \hat{\boldsymbol{z}}\}$.

2. Guidance from Continuum Modeling

We use continuum modeling as the primary theoretical motivator as well as a reference data generation tool in this work. The constitutive model we use (22, 23) has a response characterized by a rate-insensitive, nondilatant frictional flow rule when in a dense state but also models the separated state which allows material to become stress-free when below a critical density. The model has been validated in a number of previous studies of granular intrusion and locomotion (21, 25–28, 49).

The constitutive flow equations representing the material's separation behavior, shear yield condition, and tensorial codirectionality, respectively, are shown below:

$$\begin{aligned} &(\rho-\rho_c)P=0 \quad \text{and} \quad P\geq 0 \quad \text{and} \quad \rho\leq\rho_c,\\ &\dot{\gamma}\,(\tau-\mu_{\text{int}}P)=0 \quad \text{and} \quad \dot{\gamma}\geq 0 \quad \text{and} \quad \tau\leq\mu_{\text{int}}P,\\ &D_{ij}/\dot{\gamma}=\sigma'_{ij}/2\tau \quad \text{if} \quad \dot{\gamma}>0 \quad \text{and} \quad P>0, \end{aligned} \qquad [2]$$

where subscripts $i, j = 1, 2, 3$. In these equations, $\boldsymbol{\sigma}$ represents the Cauchy stress tensor and $\sigma'_{ij}=\sigma_{ij}+P\delta_{ij}$ represents the deviatoric part of $\boldsymbol{\sigma}$, where $P=-\sigma_{ii}/3$ represents the hydrostatic pressure (with summation implied over repeated indices). $\tau=\sqrt{\sigma'_{ij}\sigma'_{ij}/2}$ represents the equivalent shear stress, and μ_{int} and ρ_c represent the constant bulk friction coefficient and critical close-packed density of the granular media, respectively. $D_{ij}=(\partial_i v_j+\partial_j v_i)/2$ represents the (plastic) flow rate tensor, and $\dot{\gamma}=\sqrt{2D_{ij}D_{ij}}$ represents the equivalent shear rate. We assume that the surface friction coefficient μ_{surf} describes the interaction of the granular continuum with intruder surfaces. In general, $\mu_{\text{surf}}\leq\mu_{\text{int}}$ with $\mu_{\text{surf}}=\mu_{\text{int}}$ in the case of a fully rough interface.

We use a 3D Material Point Method (MPM) solver from Baumgarten and Kamrin (29) to implement the continuum modeling in this study, which has been successfully used for modeling complex problems in the past (29, 30). We have also validated the accuracy of the continuum model against experiments for a specific set of 3D plate intrusions, which justify the use of the continuum solver for generating 3D-RFT reference data in the final step of the model development. The details of the validation studies are provided in *Materials and Methods*.

3. Proposed Procedure: Physically Constrained Intrusion Modeling

We begin by discussing a three-step procedure which can be used to infer reduced-order intrusion models in soft media. This is followed by a derivation in Section 4 showing how these ingredients are used to deduce 3D-RFT in granular media.

Step-1: Order-Reduction Hypothesis. We assume that the intrusion stress on each surface element of the intruder is approximately equal to that of an isolated plate element in the same configuration moving the same way. This is the key order-reduction hypothesis in the RFT family of models, though other reductive hypotheses could conceivably be used.

Step-2: Apply Constraints from Continuum Description. The previous step reduces the problem to inferring a force relation on isolated plate elements. We now identify a continuum model for the media and use it to impose constraints on the intrusion force relation as implied by the continuum system. These constraints can be inferred through dimensional analysis of the model parameters and through analysis of stress state limitations in the rheology and boundary conditions.

Step-3: Apply Global Symmetry Constraints. Any function providing the intrusion force on an intruder must obey a symmetry relationship whereby if the entire problem is rotated by some amount—that is, the free surface, gravity, intruder orientation/position, and intruder velocity are all rotated the same amount—then, the resistive force must also rotate by this common global rotation. As we will show, this constraint, which implies that the drag force relations are isotropic functions of their inputs, imposes a rather strong restriction on the 3D form that 3D-RFT can take.

It is only after Steps 1 to 3 have reduced down the functional form of the intrusion model considerably that we then refer to data to fit the remaining details. Of key importance, much less fitting must be done, and one is assured that the result obeys basic physical principles when the above procedure is used. As we shall show with 3D-RFT, this procedure results in an accurate model with an explicit dependence on material parameters that can be exploited to enable rapid calibration to various granular media. Beyond granular media, in ref. 21, a pseudodiagnostic test was proposed to determine when a constitutive model for a material is likely to give rise to an accurate RFT-like intrusion model (Step 1). This "garden hoe test" examines the mathematical form of the intrusion force under the full continuum model for the case of finite-sized square intruders and compares it to the scaling of intrusion force necessarily implied by the corresponding RFT model. More discussion of this test and examples of how to use the three-step procedure in other soft materials can be found in *SI Appendix*, section S2.

In the case of granular 3D-RFT, the execution of step 2 uses the continuum model discussed previously and summarized in Eq. **2**. Assuming that the continuum model holds, the resistive force on a surface element depends on the same limited set of material parameters that govern the continuum model: ρ_c (the critical density), μ_{int} (the internal friction), and μ_{surf} (the media-surface friction). This requirement is quite constraining when combined with dimensional analysis. Also, the continuum model's lack of tensile stress states is enforced by requiring resistive stress to only have positive compressive normal component and to occur only on leading edges of the intruder. That is, only surfaces moving "into" and not "away from" a granular volume experience nonnegligible resistive force. *SI Appendix*, section S3 provides evidence in support of this hypothesis in three dimensions. We can also make inferences based on the continuum model's boundary conditions. Since the intruder is assumed to have a surface-media friction coefficient μ_{surf}, the ratio of tangential and normal stress on a surface element cannot exceed this value. In agreement with this requirement, we observe in extensive analysis of continuum model solutions that plate-tangential resistive forces generated at a higher μ_{surf} can be used to generate the tangential force for a lower μ_{surf} by simply limiting the magnitude of the tangential force based on the Coulomb friction limit. Detailed material response graphs in this regard can be found in *SI Appendix*, section S4–S5. Our extensive data analysis also allows us to assert that the normal force is relatively uninfluenced by μ_{surf} for a large range of internal friction ($\mu_{\text{int}}=0.3-0.9$) (*SI Appendix*, Fig. S3). Between different μ_{int}, the normal forces appear to vary only by a multiplicative scalar factor ξ_n as discussed in Section 4.

In addition to these premises, we will utilize a few operational constraints. We desire a 3D-RFT model that collapses back to

the previously defined 2D-RFT description in the appropriate limits. Thus, we desire to ultimately express 3D-RFT in terms of similar characteristic angles β and γ and a new twist angle ψ representing the angle between the planes of plate normal and velocity direction with the vertical, similar to the angle-based characterization of 2D-RFT by Li et al. (14) (Fig. 1*A*). Also, we limit ourselves to quasi-static intruder motions, with negligible inertial effects in the granular media. This was also assumed in the original 2D-RFT formulation and allows the force on a subsurface to be presumed independent of the surface's speed. More recently, an inertia-sensitive 2D-RFT has also been proposed and validated (25). We limit our attention to quasi-static cases in this work (see *Materials and Methods* for more details). We also require that intruders are submerged to a depth $|z|$ less than a $O(10)$ factor of the size of the intruder. This requirement comes from observations that the intrusion force stops increasing linearly with $|z|$ below a critical depth in gravity-loaded quasi-semi-infinite granular beds (24, 31); specifically, the lift component of the intrusion force saturates beneath the critical depth. This interesting phenomenon occurs even though the pressure field within the grains, excluding a localized zone about the intruder, continues increasing linearly with depth. Lastly, the RFT form assumes grains to be small relative to the size scale of the intruder. RFT is expected to have reduced accuracy along intruder surfaces that sharply vary; direct grain-size effects may be important to determining the resistive force on these subsurfaces.

4. Deducing Physically Constrained 3D-RFT

We use the previously discussed steps to propose a general form of the intended 3D-RFT model. In light of step 1, we propose a 3D-RFT that supposes that the force on any small surface element of the intruding body is equal to what the force would be if the plate element were isolated and moving on its own. Hence, the force (per area per depth, $\boldsymbol{\alpha}$) is a function that depends only on the element's surface normal $\hat{\boldsymbol{n}}$, local velocity direction $\hat{\boldsymbol{v}}$, and depth $|z|$, along with the acceleration of gravity $\boldsymbol{g}$ and material properties "mat," such that the total intrusion force satisfies

$$\boldsymbol{F}^{\text{total}} = \int_{\text{surf}} \boldsymbol{\alpha}(\hat{\boldsymbol{n}}, \hat{\boldsymbol{v}}, \boldsymbol{g}, |z|; mat)\, |z|\, ds. \qquad [3]$$

Referring to Step 2, the material properties are taken to be given by the parameter set $mat = \{\rho_c, \mu_{\text{int}}, \mu_{\text{surf}}\}$. Assuming for the time being that the intruder is fully rough, $\mu_{\text{surf}} = \mu_{\text{int}}$, dimensional analysis together with the observed dependence on μ_{int} in *SI Appendix*, Fig. S3 reduces the functional dependence of $\boldsymbol{\alpha}$ significantly, requiring that

$$\boldsymbol{\alpha} = \rho_c g \tilde{f}(\mu_{\text{int}})\, \boldsymbol{\alpha}^{\text{gen}}(\hat{\boldsymbol{n}}, \hat{\boldsymbol{v}}, \hat{\boldsymbol{g}}), \qquad [4]$$

where $\boldsymbol{g} = g\hat{\boldsymbol{g}}$, the dimensionless function $\tilde{f}$ is as-yet undetermined, and the prefactor $\rho_c g \tilde{f}(\mu_{\text{int}})$, which we collectively refer to as ξ_n, is a media-dependent scaling coefficient reflecting the overall intrusive strength of the system. The generic RFT function $\boldsymbol{\alpha}^{\text{gen}}$ is labeled as such because, under the given premises, it is universal across all granular/intruder systems with fully rough interfaces. We now show how $\boldsymbol{\alpha}^{\text{gen}}$ can be used to enable the modeling non–fully rough surfaces.

We can uniquely decompose the vector-valued function $\boldsymbol{\alpha}^{\text{gen}}$ into normal and tangential directions as $\boldsymbol{\alpha}^{\text{gen}} \equiv \boldsymbol{\alpha}_n^{\text{gen}} + \boldsymbol{\alpha}_t^{\text{gen}}$. We may now remove the fully rough assumption and suppose $\mu_{\text{surf}} \neq \mu_{\text{int}}$. Then, in accord with the surface friction limit and conclusions drawn from *SI Appendix*, section S5, we can simply scale down the tangential component of surface stress from the fully rough case to the surface friction μ_{surf} limit by writing

$$\boldsymbol{\alpha} = \rho_c g \tilde{f}(\mu_{\text{int}}) \left[\boldsymbol{\alpha}_n^{\text{gen}} + \min\left(\frac{\mu_{\text{surf}} |\boldsymbol{\alpha}_n^{\text{gen}}|}{|\boldsymbol{\alpha}_t^{\text{gen}}|},\, 1 \right) \boldsymbol{\alpha}_t^{\text{gen}} \right]. \qquad [5]$$

The 3D-RFT model we are proposing is closed upon choosing the scalar-valued function $\tilde{f}(\mu_{\text{int}})$ and the vector-valued function $\boldsymbol{\alpha}^{\text{gen}}(\hat{\boldsymbol{n}}, \hat{\boldsymbol{v}}, \hat{\boldsymbol{g}})$. Upon selection of these two functions, Eq. **5** can be used to determine $\boldsymbol{\alpha}$ for any choice of material and interface properties $\{\rho_c, \mu_{\text{int}}, \mu_{\text{surf}}\}$.

We now apply symmetry constraints inherent to the drag problem (Step 3) to further constrain the functional form of $\boldsymbol{\alpha}^{\text{gen}}$. Our strategy is to constrain the function space to satisfy symmetry constraints by design rather than leaving it to chance based on the choice of fit functions. Moreover, by enforcing the symmetry constraints directly, we reduce the space of admissible functions, thereby reducing the amount of fitting that must be done.

Consider a small plate intruder characterized with $\hat{\boldsymbol{n}}$, $\hat{\boldsymbol{v}}$, ds, $|\boldsymbol{z}|$, and $\boldsymbol{g}$. For $\mu_{\text{surf}} = \mu_{\text{int}}$, the force on the plate according to RFT is $\boldsymbol{dF} = \xi_n \boldsymbol{\alpha}^{\text{gen}}(\hat{\boldsymbol{n}}, \hat{\boldsymbol{v}}, \boldsymbol{g})|z|ds$. If the entire system is rotated—including the intruder, the granular bed, and gravity—the resistive force on the intruder must rotate by the same amount. This is because rotating the entire system should be consistent with a fixed system and a rotation of the observer. Fig. 2*A* visualizes this action; note that the distance to the free surface along the gravity vector ($|z|$) remains unchanged as does the plate area (ds). Thus, for any rotation $\boldsymbol{R}$, we expect that $\boldsymbol{R}\,\boldsymbol{dF} = \xi_n \boldsymbol{\alpha}^{\text{gen}}(\boldsymbol{R}\hat{\boldsymbol{n}}, \boldsymbol{R}\hat{\boldsymbol{v}}, \boldsymbol{R}\hat{\boldsymbol{g}})|z|\, ds$, and thus

$$\boldsymbol{\alpha}^{\text{gen}}(\boldsymbol{R}\hat{\boldsymbol{n}}, \boldsymbol{R}\hat{\boldsymbol{v}}, \boldsymbol{R}\hat{\boldsymbol{g}}) = \boldsymbol{R}\boldsymbol{\alpha}^{\text{gen}}(\hat{\boldsymbol{n}}, \hat{\boldsymbol{v}}, \hat{\boldsymbol{g}}). \qquad [6]$$

This "global rotation constraint" implies that $\boldsymbol{\alpha}^{\text{gen}}$ is an isotropic function of its inputs. Thus, in accord with isotropic representation theory (IRT) (32), the function must have the following specific form:

$$\boldsymbol{\alpha}^{\text{gen}}(\hat{\boldsymbol{n}}, \hat{\boldsymbol{v}}, \hat{\boldsymbol{g}}) = f_1 \hat{\boldsymbol{n}} + f_2 \hat{\boldsymbol{v}} + f_3 \hat{\boldsymbol{g}}, \qquad [7]$$

where f_1, f_2, and f_3 are three mutually independent arbitrary scalar-valued functions of coordinate-invariant dot-products between the three direction vectors, that is, $f_i = f_i(\hat{\boldsymbol{g}}\cdot\hat{\boldsymbol{v}}, \hat{\boldsymbol{g}}\cdot\hat{\boldsymbol{n}}, \hat{\boldsymbol{n}}\cdot\hat{\boldsymbol{v}})$. Eq. **7** has reduced the problem of fitting $\boldsymbol{\alpha}^{\text{gen}}$ from determining a vector-valued function of six independent variables (three vectors, each with a constraint of being unit magnitude) to determining a vector-valued function of three independent variables (three dot products). Note that the form given in Eq. **5** for general μ_{surf} continues to satisfy the IRT requirement Eq. **7**. A detailed proof in this regard is provided in *SI Appendix*, section S6.

We next introduce the methodology for parametrizing subsurfaces in terms of three angles to arrive at our ultimate description of $\boldsymbol{\alpha}^{\text{gen}}$.

3D-RFT Subsurface Characterization. Eq. **7** defines the normalized stress-per-depth on a subsurface using $\hat{\boldsymbol{n}}$, $\hat{\boldsymbol{v}}$, and $\hat{\boldsymbol{g}}$ directions and corresponding dot products. We could stop here and set out to fit the f_i functions; however, there are certain advantages to first reexpressing Eq. **7** in terms of an orthogonal set of directions and angles measured from those directions. Using angles helps us meet

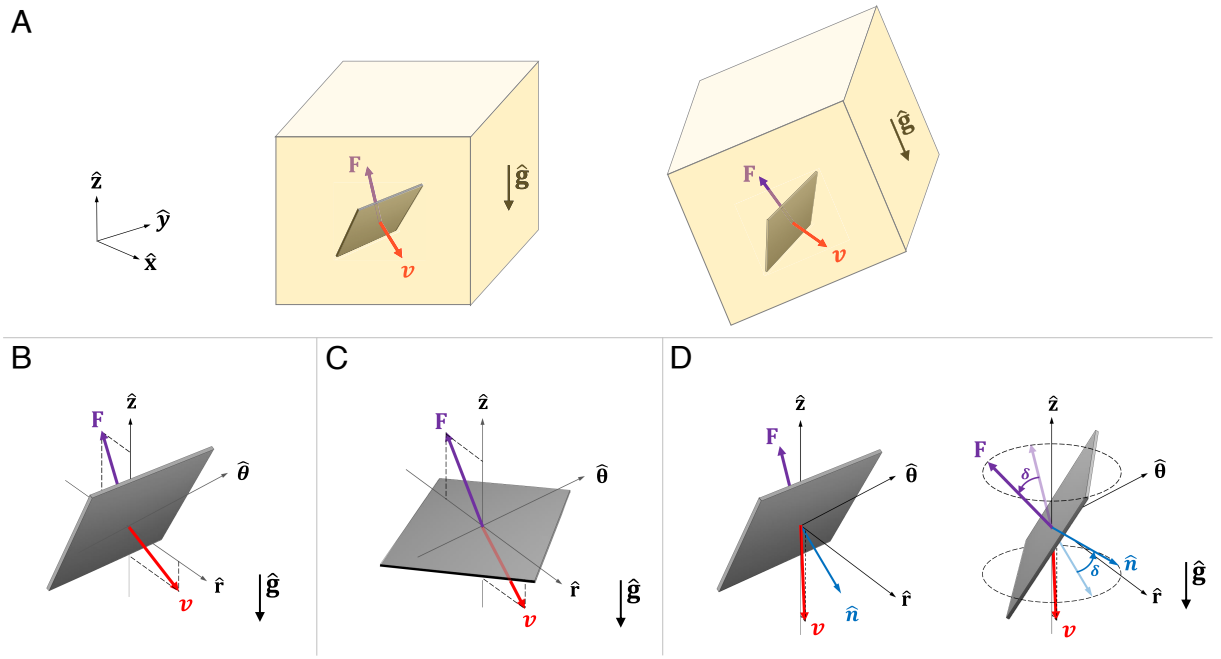

Fig. 2. 3D-RFT symmetry constraints: (*A*) Global rotational constraint requiring the drag force to be an isotropic function of the plate normal, motion direction, and gravity direction. Some consequences of this constraint are plate twist symmetry, plate tilt symmetry, and vertical motion symmetry. (*B*) A special case of plate twist symmetry: $F_\theta(\beta, \gamma, \psi = 0) = 0$. (*C*) A special case of plate tilt symmetry: $F_\theta(\beta = 0, \gamma, \psi) = 0$, and (*D*) Vertical motion symmetry: $(\beta, \gamma = \pm\pi/2, \psi = 0) \rightarrow (\beta, \gamma = \pm\pi/2, \psi = \delta)$ causes $(F_r, F_\theta = 0, F_z) \rightarrow (F_r \cos\delta, F_r \sin\delta, F_z)$. Violet, red, and blue arrows show force, velocity, and surface-normal direction, respectively.

our desire to maintain a consistency of 3D-RFT with the 2D-RFT form, which is also angle-based, and using an orthogonal basis rather than the set $\{\hat{\boldsymbol{n}}, \hat{\boldsymbol{v}}, \hat{\boldsymbol{g}}\}$ eases the physical interpretation and simplifies calibration.

We define a local cylindrical coordinate system at each surface element as follows (Fig. 1*C*): We choose the direction opposite to the gravity (upward in general) as the positive z-direction and use the horizontal component of $\hat{\boldsymbol{v}}$ as the positive $\hat{\boldsymbol{r}}$ direction. The remaining $\hat{\boldsymbol{\theta}}$ direction is chosen as the cross product between $\hat{\boldsymbol{r}}$ and $\hat{\boldsymbol{z}}$. The free surface is taken as the reference ($z = 0$) for the z-direction.* Next, we recast Eq. 7 in terms of angles referenced against directions $\{\hat{\boldsymbol{r}}, \hat{\boldsymbol{\theta}}, \hat{\boldsymbol{z}}\}$. The surface twist angle, ψ, gives the azimuthal angle between the r-axis and the projection of the surface normal onto the $r\theta$-plane, denoted by $\hat{\boldsymbol{n}}_{r\theta}$. The surface tilt angle, β, is the polar angle between the r-axis and the $r\theta$-plane. To be clear, β measures the angle between the $r\theta$-plane and one of $\hat{\boldsymbol{n}}$ or $-\hat{\boldsymbol{n}}$, whichever gives a result in the $[-\pi/2, \pi/2]$ range. This choice is not problematic because at any time, only one side of a plate element experiences forces, and this can be identified using the leading edge condition $(\hat{\boldsymbol{v}} \cdot \hat{\boldsymbol{n}} \geq 0)$. The local coordinate frame definitions keep the velocity vector completely within the rz-plane. Thus, once $\{\hat{\boldsymbol{r}}, \hat{\boldsymbol{\theta}}, \hat{\boldsymbol{z}}\}$ are determined, only one angle is needed to represent the velocity direction. This angle of attack, γ, is the angle between the velocity direction vector and the local positive r-axis. See Fig. 1*C* for a visual representation of these angles. Based on the above definitions, the variations of each of the systems' characteristic angles $\{\beta, \gamma, \psi\}$ is restricted to $[-\pi/2, \pi/2]$ for any leading-edge surface. We use these limits in the generation of reference 3D-RFT data. Mathematical formulae for the angles in terms of vector components in a fixed cartesian frame are provided in *SI Appendix*, section S7. With some algebra, one can express the $\{\hat{\boldsymbol{n}}, \hat{\boldsymbol{v}}, \hat{\boldsymbol{g}}\}$ basis vectors in terms of $\{\hat{\boldsymbol{r}}, \hat{\boldsymbol{\theta}}, \hat{\boldsymbol{z}}\}$, and the three angles (*SI Appendix*, Eq. 9). Substituting the result into Eq. 7 yields the expressions for the components of $\boldsymbol{\alpha}^{\text{gen}} = \alpha_r^{\text{gen}}\hat{\boldsymbol{r}} + \alpha_\theta^{\text{gen}}\hat{\boldsymbol{\theta}} + \alpha_z^{\text{gen}}\hat{\boldsymbol{z}}$ as follows:

$$\begin{aligned}
\alpha_r^{\text{gen}}(\beta, \gamma, \psi) &= f_1 \sin\beta \cos\psi + f_2 \cos\gamma, \\
\alpha_\theta^{\text{gen}}(\beta, \gamma, \psi) &= f_1 \sin\beta \sin\psi, \\
\alpha_z^{\text{gen}}(\beta, \gamma, \psi) &= -f_1 \cos\beta - f_2 \sin\gamma - f_3,
\end{aligned} \qquad [8]$$

where $f_i = f_i(\hat{\boldsymbol{g}} \cdot \hat{\boldsymbol{v}}, \hat{\boldsymbol{g}} \cdot \hat{\boldsymbol{n}}, \hat{\boldsymbol{n}} \cdot \hat{\boldsymbol{v}})$ are three as-yet undetermined functions of the three dot products, which are now given by the three angles as follows:

$$\begin{aligned}
\hat{\boldsymbol{g}} \cdot \hat{\boldsymbol{v}} &= \sin\gamma\,, \qquad \hat{\boldsymbol{g}} \cdot \hat{\boldsymbol{n}} = \cos\beta, \\
\hat{\boldsymbol{n}} \cdot \hat{\boldsymbol{v}} &= \cos\psi \cos\gamma \sin\beta + \sin\gamma \cos\beta.
\end{aligned} \qquad [9]$$

Eqs. **8** and **9** give the final functional form of $\boldsymbol{\alpha}^{\text{gen}}$ and the completion of the three-step process outlined in Section 4. The 3D-RFT model we introduce is closed upon fitting the three f_i as functions of the three dot products, which we shall do in the next section using a targeted set of in silico reference tests. Note that by building the angle dependences of α_r^{gen}, $\alpha_\theta^{\text{gen}}$, and α_z^{gen} indirectly from the f_i using IRT rather than by directly fitting the α^{gen} functions, the model is guaranteed to satisfy many easy-to-observe requirements regardless of how the f_i are picked. These include (i) "plate twist symmetry" (Fig. 2*B*), which requires that the subsurface forces in the r- and z-direction should be even functions of plate twist (ψ) and that force in the θ-direction should be an odd function of ψ; (ii) "plate tilt symmetry" (Fig. 2*C*) which requires that when the plate faces upward or downward ($\beta = 0$), the subsurface force in the θ-direction should

*When $|\boldsymbol{v} - (\boldsymbol{v} \cdot \hat{\boldsymbol{z}})\hat{\boldsymbol{z}}|$ is zero (a subsurface moves up or down), $\hat{\boldsymbol{r}}$ is set to the direction of the horizontal component of the surface normal, i.e., $\hat{\boldsymbol{r}} = (\hat{\boldsymbol{n}} - (\hat{\boldsymbol{n}} \cdot \hat{\boldsymbol{z}})\hat{\boldsymbol{z}})/|\hat{\boldsymbol{n}} - (\hat{\boldsymbol{n}} \cdot \hat{\boldsymbol{z}})\hat{\boldsymbol{z}}|$.

vanish, the force magnitude should depend only on γ, and the twist angle ψ should have no influence on the force; (iii) "vertical motion symmetry" (Fig. 2*D*), which requires that for any tilt β, as $\gamma \to \pm\pi/2$ (approaching an upward or downward motion) any azimuthal rotation (changing ψ at constant β) of a subsurface should rotate the resultant force on the subsurface by the same angle. Moreover, by using Eqs. **8** and **9**, we are ensured that the relation for $\boldsymbol{\alpha}^{\text{gen}}$ always has the correct periodicity in the three angles.

5. Reference Data

We use a large number of combinations (~3,000) of material properties (μ_{int} and μ_{surf}) and 3D-RFT angles (β, γ, and ψ) to generate a bank of continuum modeling-based reference data for evaluating the 3D-RFT form. The details of the combinations are provided in *SI Appendix*, section S4. Based on this extensive data set, we can fit the functions f_1, f_2, and f_3 that determine $\boldsymbol{\alpha}^{\text{gen}}$, and we can also fit $\tilde{f}$. Fig. 3 *A–D* shows the simulation setup used for the data collection. While both the β and the γ angles are varied over the interval $[-\pi/2, \pi/2]$, ψ was varied only in $[0, \pi/2]$ taking advantage of "plate twist symmetry" discussed earlier.

Fig. 3*E* shows a comparison of reference data to an example fitting of 3D-RFT. Odd columns in the figure show the data obtained using continuum simulations as a function of β and γ at four ψ values. The material properties were $\mu_{\text{int}} = 0.4$, $\rho_c = 3{,}000$ kg/m^3, and $\mu_{\text{surf}} = 0.15$. Corresponding 3D-RFT fittings are plotted on the even columns. We find the value of the scaling coefficient ξ_n to be 0.92×10^6 N/m^3 for this material. While Eq. **8** represents the most generic form of 3D-RFT, the choice of the functions f_i determines the final 3D-RFT model. All the results presented in this work use third degree polynomial fits for the f_i functions (*SI Appendix*, Table S3). Higher-order polynomials could be used, which can better fit the reference data. We provide one such form in (*SI Appendix*, Table S4). The performance of 3D-RFT does not change significantly between third and fourth degree polynomial fits. The latter form fits the trends of $|\boldsymbol{\alpha}_t|/|\boldsymbol{\alpha}_n|$ better but has inconsequential effects on 3D-RFT predictions for the test cases used in this study.

The 3D-RFT model we propose is completed using a cubic $\tilde{f}$ fit as shown in *SI Appendix*, Fig. S4—this dependence is in accord with observations of past researchers in the simpler vertical intrusion of flat plates (33)—and with $\boldsymbol{\alpha}^{\text{gen}}$ expressed using Eq. **8** in terms of third-degree polynomial fits for the f_i, and using directions $\{\hat{\boldsymbol{r}}, \hat{\boldsymbol{\theta}}, \hat{\boldsymbol{z}}\}$ and angles $\{\beta, \gamma, \psi\}$ as shown in Fig. 3 *A–D*. To numerically implement the model, we discretize the intruder surface into small plate elements and determine $\{\beta, \gamma, \psi\}$ and $\{\hat{\boldsymbol{r}}, \hat{\boldsymbol{\theta}}\}$ for each element. The model then provides the force on each element that is on the leading edge of the intruder. A step-by-step implementation strategy for 3D-RFT is given in *SI Appendix*, section S7.

6. Validation Studies

We first test the accuracy of the implied localization of the proposed form of 3D-RFT (Eq. **3**) as well as the f_i fits by comparing predictions for 10 arbitrary intruding objects to full continuum model solutions of the same intrusions. We use the continuum material properties $\mu_{\text{int}} = 0.4$, $\rho_c = 3{,}000$ kg/m^3, and $\mu_{\text{surf}} = 0.4$ for these cases. A representation of the objects and their dimensions is provided in Fig. 4 and its caption. The object length scales are kept as 7 cm in all the cases, and the objects are submerged to an initial depth of 27 cm (vertical distance between the free surface and the geometric center of the shape). The objects are translated at a speed of 0.1 m/s in different directions in the xz-plane. These directions are characterized using θ, which represents the angle between the velocity direction and the positive x-axis in a clockwise direction (same as γ definition for a plate element). Negative θ represents upward motion, positive θ represents downward motion, and $\theta = 0$ represents horizontal motion along the x-direction. The variations of net-force (F_x, F_y, and F_z) with θ are plotted in Fig. 4. 3D-RFT agrees with the continuum solutions well in modeling all the intrusion test scenarios considered in Fig. 4. Objects with sharp corners generally show weaker fits than those with smoother shapes; this could be because sharp corners are difficult to represent with our material point method.

Validation of 3D-RFT with Detailed DEM Studies. We further check the performance of 3D-RFT with two DEM studies. In these studies, we measure net moment, net force, and resistive force distribution on bodies intruding into granular volumes with simultaneous rotation and translation velocities. We use a 50/50 mixture of 3 mm and 3.4 mm diameter grains with a grain density of 2,470 kg/m^3, and the granular volumes have an effective bulk density of 1,310 kg/m^3 ($\phi \approx 0.53$) in both the DEM studies. Below, we use d to denote the larger grain size. We determine the internal coefficient of friction μ_{int} as 0.21 using simple shear simulations. *SI Appendix*, section S8 provides more details of the simple shear test setup and detailed material properties. Using this value together with the known $\tilde{f}$ relationship, we obtain a scaling coefficient (ξ_n) value of 0.12×10^6 N/m^3. See *SI Appendix*, Table S1 and section S4 for more details.

Cylinder drill. In this test, we model simultaneous rotation and translation (drilling) of a solid cylindrical intruder along the z-axis (vertically down) in a granular volume (diameter = 0.05 m, length = 0.14 m). The cylinder axis was kept in the horizontal plane throughout the motion. The setup consists of approximately 6×10^5 particles in a $100d \times 100d \times 70d$-sized granular bed. The setup dimensions and setup schematic are provided in Fig. 5. The figure also shows the variations of force and moment on the intruder over time from the DEM studies versus 3D-RFT. In addition, the figure shows the variation of stress over the intruder surface from DEM and 3D-RFT. All reported components (net force and moment, as well as stress distributions) show a strong match between the two approaches.

Bunny drill. In this test, we model the drilling motion ($\omega = 2\pi$ rad/s, $v = 0.1$ m/s) of a Stanford bunny (34) in a granular volume. The shape is chosen because it is an example of a complex, asymmetric 3D object. The granular bed consists of approximately 2.1×10^6 particles filling a $150d \times 150d \times 88d$-sized domain. The bunny shape was slightly modified from the standard shape—the shape was proportionally scaled in such a way that the bunny height measures 0.1 m, and the bunny base was flattened to make the base a plane surface without an inward extrusion. Fig. 6 shows the simulation setup where the grains are colored with velocity magnitudes. Fig. 6 also shows the variation of stresses over the intruder surface from DEM and 3D-RFT. All the reported components (net force and moment as well as stress distributions) show a strong match between the two approaches.

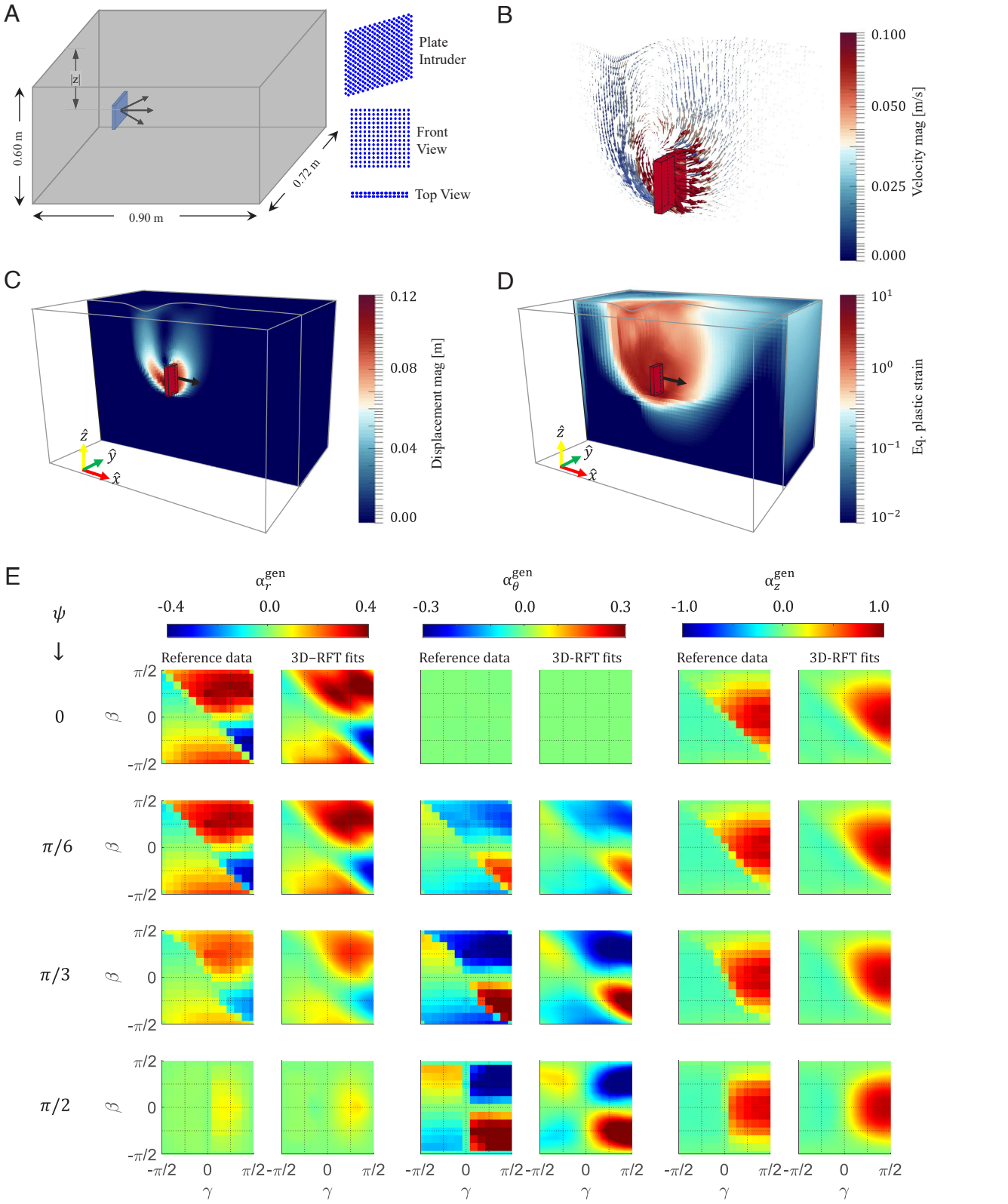

Fig. 3. Reference data collection and sample 3D-RFT fitings: MPM is used to simulate the continuum model for reference data collection. (*A*) Schematic of intrusion setup with the thin plate (0.105 m × 0.105 m × 0.015 m) used for data collection. Variation of (*B*) material flow, (*C*) displacement magnitude, and (*D*) equivalent plastic strain magnitude from one of the test setups. (*E*) Reference data for normalized forces ($|\boldsymbol{F}/A|\boldsymbol{z}|\xi_n|$) and 3D-RFT functional fittings ($|\alpha^{\text{gen}}_{r,\theta,z}|$) for plate intrusions at various plate twists ($\psi = [0, \pi/6, \pi/3, \pi/2]$ rad), plate inclinations ($\beta = -\pi/2 : \pi/6 : \pi/2$ rad), and velocity directions ($\gamma = -\pi/2 : \pi/6 : \pi/2$ rad) for a material with $\mu_{\text{int}} = 0.4$, $\rho = 3{,}000$ kg/m^3, and $\mu_{\text{surf}} = 0.15$. The reference data are normalized with $\xi_n = 0.92 \times 10^6$ N/m^3.

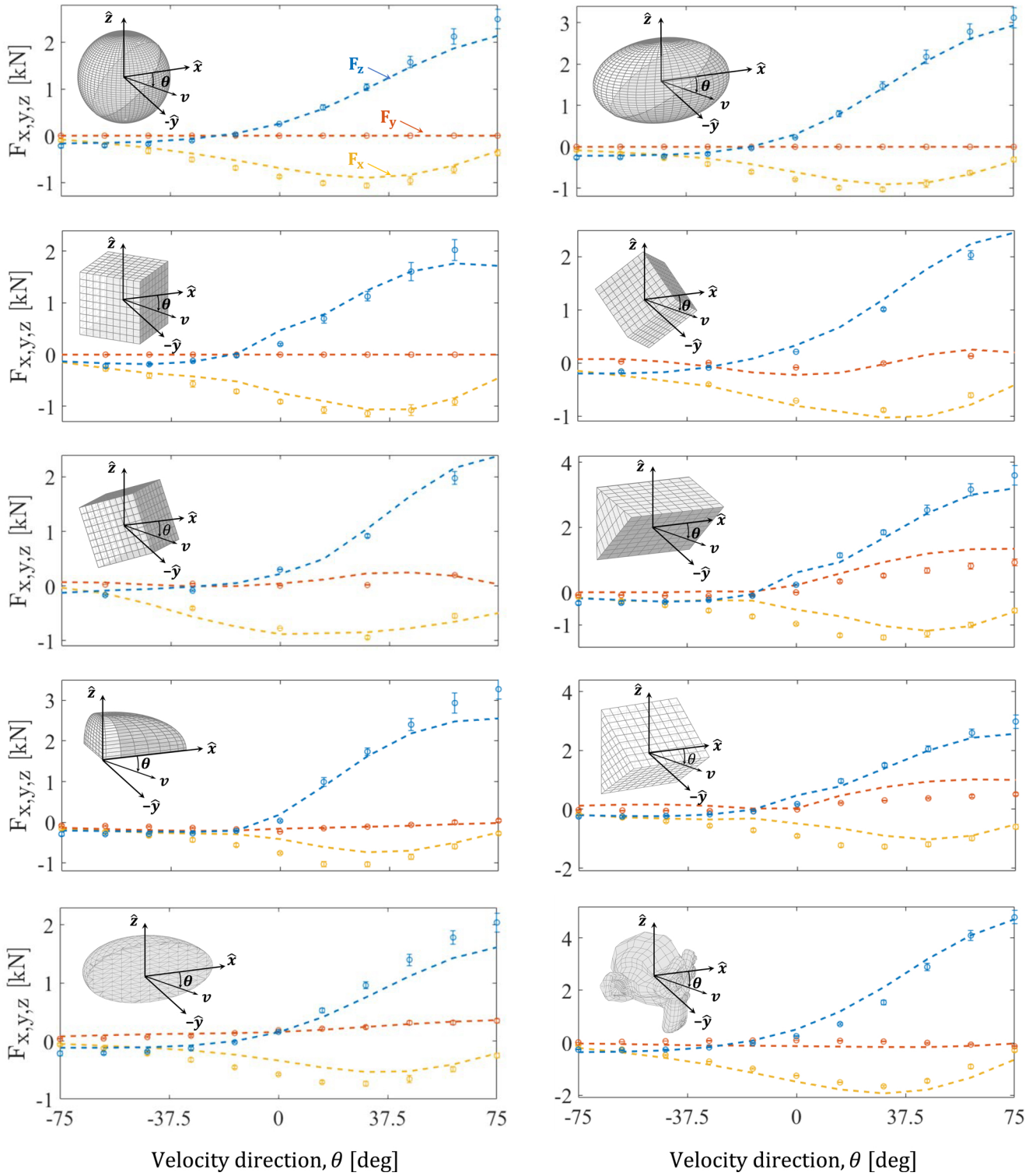

Fig. 4. 3D-RFT verification studies 1-10: Variation of different force components (F_x: yellow, F_y: orange, and F_z: blue) during motions of various rigid objects (intruders) obtained from continuum modeling ("o" markers) and 3D-RFT (dashed lines) at various velocity directions. All the studies were conducted at a velocity magnitude of 0.1 m/s. All the velocities completely lie in the $xz-$plane. A pictorial representation of each intruder is provided in the corresponding subfigure. The intruder shapes include (1) a 5-cm radius sphere, (2) an ellipsoid with [7.5, 4.5, 4.5]-cm semi-axes (x,y,z), (3) a 7.5-cm-tilted cube, rotated from a cartesian alignment by $\pi/4$ radians about the z-axis, (4) a 7.5-cm cube sequentially rotated by $\pi/3$ and $\pi/4$ radians along the y-axis and z-axis from a cartesian alignment, (5) a 7.5 cm cube sequentially rotated by $\pi/6$ and $\pi/3$ radians along the y-axis and z-axis from a cartesian coordinate alignment, (6) an isosceles right angle prism with 7.5-cm equal sides and 10.5-cm width, (7) a quarter ellipsoid with [7.5, 4.5, 4.5]-cm semi-axes (x,y,z) ($x > 0$ and $y > 0$), (8) an isosceles right angle prism with equal sides of 10.5 cm and 7.5 cm width, (9) a half-ellipsoid with [7.5, 4.5, 4.5]-cm semi-axes (x,y,z) ($y > 0$), and (10) a monkey-head shape from the open-source 3D computer graphics software "Blender" at a scale factor of 0.075 and facing $\pi/4$ radians from the positive x-direction in the xy-plane.

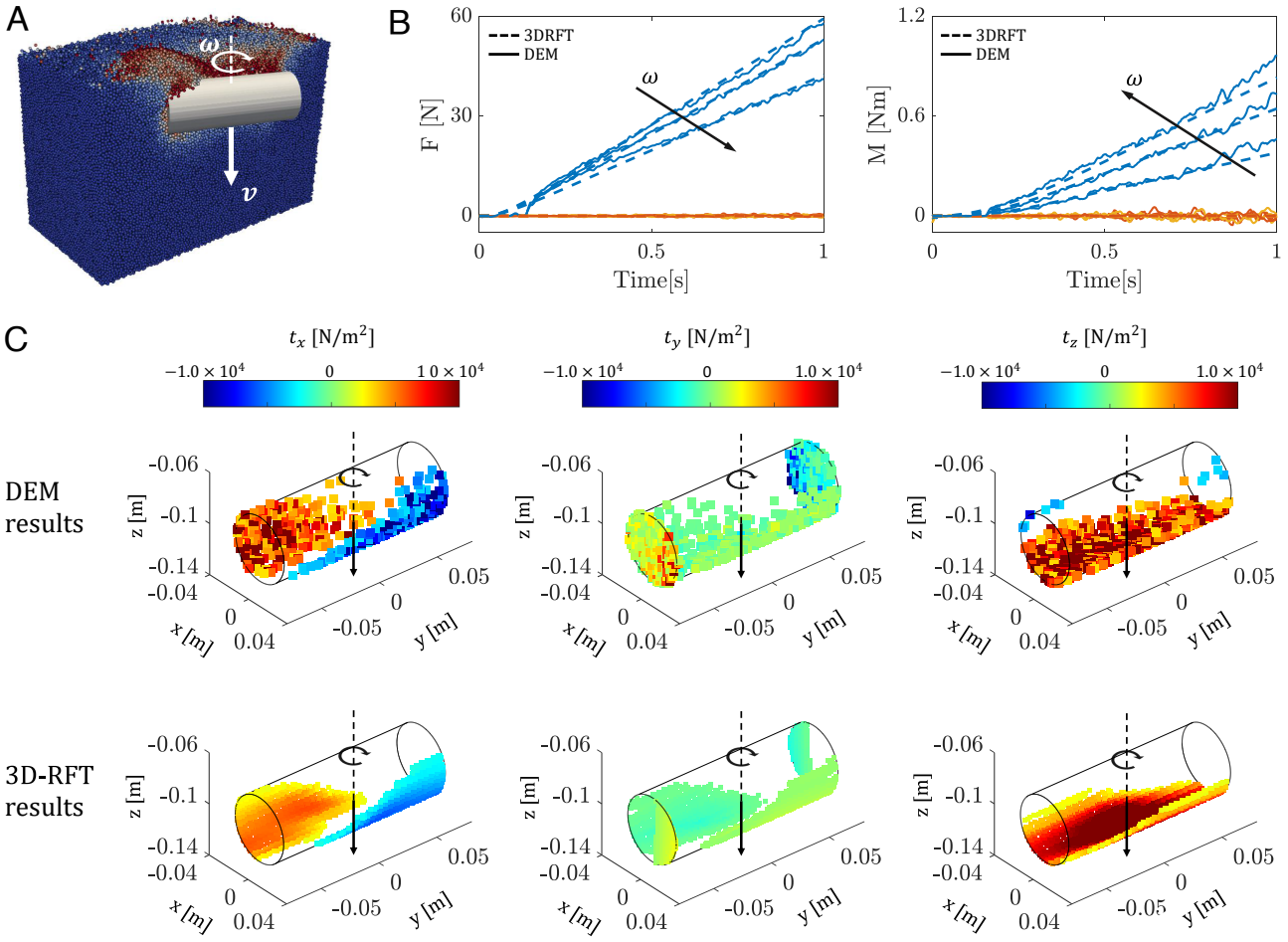

Fig. 5. DEM-based 3D-RFT verification—cylinder drill: (*A*) A snapshot of the cylinder drill setup where a 50-mm diameter and 140-mm length cylinder was simultaneously rotated (ω, clockwise) and translated (v, downward) along the z-axis. We use three combinations of (ω, v): $[(0.25\pi, 0.1), (0.5\pi, 0.1), (\pi, 0.1)]$ (rad/s,m/s). Black arrows in (*B*) show the direction of increasing ω in each graph. The grains are colored with velocity magnitudes. The simulation domain consisted of $\sim 6 \times 10^5$ particles (50/50 mix of 3-mm and 3.4-mm diameter (d) grains) spread over $100d \times 100d \times 70d$ physical space. (*B*) Variation of net force (*F*, *Left*) and moment (*M*, *Right*) components (x: yellow, y: orange, and z: blue) from DEM (solid lines) and 3D-RFT (dotted lines) for $\omega = \pi$ rad/s. (*C*) Variation of various force components from DEM (*Top*) and 3D-RFT (*Bottom*) at a 10-cm depth below the free surface ($t = 1$s). The DEM material properties are provided in *SI Appendix*, Table S2.

7. Conclusion

This work proposes a mechanistic framework for developing reduced-order models in soft materials. Successful development of a granular 3D-RFT indicates the robustness of the approach for these purposes. The 3D-RFT developed herein is an important step toward developing a generic real-time modeling technique capable of modeling granular intrusion of arbitrarily shaped objects over a large range of low and high-speed scenarios in diverse materials and environments. Previously, granular RFT's usage has focused on the modeling of arbitrary 2D objects moving in-plane. We have proposed an extension of RFT to three dimensions in a fashion consistent with granular continuum mechanics and necessary symmetry constraints. The accuracy of the proposed 3D-RFT was demonstrated against a variety of full-field intrusion simulations, both continuum and DEM. Notably, we provide a scheme that determines 3D-RFT in different intrusion systems quickly and directly in terms of basic properties of the granular media (ρ_c and μ_{int}) and the intruder surface (μ_{surf}).

The most immediate opportunity to expand 3D-RFT would be to combine 3D-RFT with dynamic RFT (25) to build a high-speed three-dimensional RFT (3D-DRFT). The current form of 3D-RFT does not include a "shadowing effect;" i.e., the fact that forces are reduced on leading edge surfaces that lie in the immediate wake behind another part of the intruder (35). Such effects are more pronounced in intruders with complex shapes or fine geometric features such as the bunny shape we consider in this study. Characterizing this effect would be an important addition to RFT. Effects of multibody intrusions (24, 36), density variations (37), inertial and noninertial velocity effects (3, 25, 38), cohesion (39, 40), and inclined domains (41) on the resistive forces experienced by intruding bodies are among other aspects for further exploration toward the ultimate goal of a generic and fast granular intrusion model applicable to terradynamical motions (8), granular impact systems (42, 43), locomotors (44), and many other similar applications.

The three-step mechanistic approach that produced 3D-RFT could be extended to produce intrusion models in other soft materials, including possible applications in colloids, gels, and biological media. We refer readers to *SI Appendix*, section S2 to see demonstrations of the procedure being used in other common materials and a discussion on determining the accuracy of the RFT localization rule (Step 1) in other media.

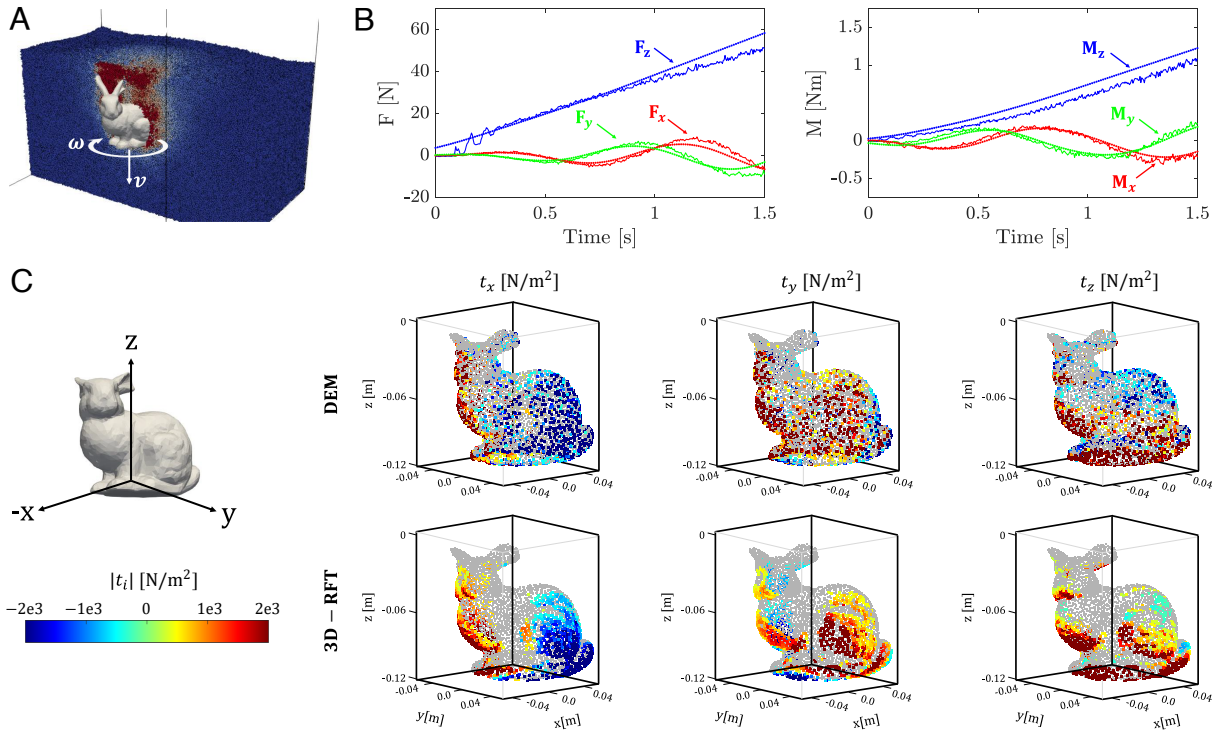

Fig. 6. DEM-based 3D-RFT verification—bunny drill: (*A*) A snapshot of the Stanford bunny drill setup where a 10-cm-high Stanford bunny was simultaneously rotated ($\omega = 2\pi$rad/s, clockwise) and translated ($v = 0.1$ m/s, downward) along the *z*-axis. The grains are colored with velocity magnitudes. The simulation domain consisted of $\sim 2.1 \times 10^6$ particles (50/50 split of 3 mm and 3.4 mm diameter (d) grains) spread over a $150d \times 150d \times 88d$ physical space. (*B*) Variation of net force (*F*, *Left*) and moment (*M*, *Right*) components (*x*: yellow, *y*: orange, and *z*: blue) from DEM (solid lines) and 3D-RFT (dotted lines). (*C*) Components of the surface stress distribution from DEM (*Top*) and 3D-RFT (*Bottom*) at a 5-cm bunny-center-depth below the free surface. The DEM material properties are provided in *SI Appendix*, Table S2.

Materials and Methods

Evaluation of Quasi-static Conditions in a System. We use the following definitions of the microinertial number I and the macroinertial number I_{mac} for evaluating the applicability of 3D-RFT in modeling the granular resistive forces in a granular intrusion system:

$$I = \dot{\gamma}/\sqrt{P/\rho_g d^2}, \qquad I_{\text{mac}} = v/\sqrt{P/\rho_g},$$

where $\dot{\gamma}$ represents the material shear rate, P represents the hydrostatic pressure, ρ_g represents the material grain density, d represents the mean grain diameter, and v represents the speed. The I_{mac} formulation is equivalent to the inverse square root of the Euler number which measures the ratio of the dynamic pressure ρv^2 to the total pressure P.

The macroinertial and microinertial numbers are defined pointwise within a granular media, so to determine whether an intrusion is quasi-static, it is convenient to determine characteristic values for these numbers. For this, we use characteristic values of $\dot{\gamma}$, P, and v. We assume that the intruder has an angular velocity ω, a translational velocity v_{intru}, and a characteristic length L. We also assume that the media has a critical density ρ_c and that the system is acted upon by gravity g. We characterize v as $v = \max(v_{\text{intru}}, L\omega/2)$ and $\dot{\gamma}$ as $\dot{\gamma} = v/L$. We consider intrusive loading of the system at characteristic depth L to give a characteristic P as $\xi_n L$. Upon substitution, we get the following:

$$I \sim (v/L)/\sqrt{(\xi_n L)/\rho_g d^2} = \sqrt{\frac{v^2 \rho_g d^2}{\xi_n L^3}} = \frac{vd}{L}\sqrt{\frac{\rho_g}{\xi_n L}},$$

$$I_{\text{mac}} \sim v/\sqrt{\xi_n L/\rho_g} = v\sqrt{\frac{\rho_g}{\xi_n L}}.$$

From the above equations, we observe that the characteristic value of I_{mac} reduces to a multiple of the Froude number (Fr) in gravity-loaded systems. To this end, Sunday et al. (45) explored the existence of macroinertial effects during high-speed granular intrusions and observed insignificant contributions of macroinertial effects in the material force response for $Fr < 1.5$, which gives $I_{\text{mac}} \lessapprox 0.48$. Similarly, Agarwal et al. (25), observed insignificant macroinertial effects (macroinertial forces $< 10\%$ of static resistive forces i.e. $\rho A v^2/K|z| < 10\%$) in granular plate intrusions at $I_{\text{mac}} < 0.16$. Thus, we impose an upper limit of 0.15 on I_{mac} to be quasi-static. The degree that I affects the flow can be quantified by how much it changes the apparent internal friction (46, 47). To keep these changes bounded by 10%, we set an upper bound on the characteristic value of I to be 0.010 so as to ensure quasi-static conditions. For all the test cases used in this study, we choose system parameters in such a way that I and I_{mac} are always below the abovementioned limits keeping their motions in quasi-static limits. The test cases 1 to 10 are continuum simulations that use a rate-independent constitutive law and have $I_{\text{mac}} \sim 0.02$ ($L \approx 0.07$ m, $v = 0.1$ m/s, $\xi_n = 0.92 \times 10^6$, $\rho_c = 3{,}000$ kg/m^3). In the DEM-based cylinder drill test cases, we find $I < 0.002$ and $I_{\text{mac}} < 0.07$ ($L \approx 0.10$ m, $\omega < \pi$ rad/s, $v_{\text{intruder}} = 0.1$ m/s, $\xi_n = 0.12 \times 10^6$, $\rho_g = 2{,}470$ kg/m^3). Similarly, in the bunny drill test case, we find $I \approx 0.004$ and $I_{\text{mac}} \sim 0.13$ ($L \approx 0.10$ m, $\omega = 2\pi$ rad/s, $v_{\text{intruder}} = 0.1$ m/s, $\xi_n = 0.12 \times 10^6$, $\rho_g = 2{,}470$ kg/m^3). Thus, 3D-RFT is a valid approach for modeling all the test cases considered in this study, based on the insignificance of microinertial and macroinertial force contributions.

Continuum Approach Accuracy Validation. Several studies in the past have verified the accuracy of this constitutive formulation in plane-strain problems (2D). We use the 3D numerical implementation of MPM developed by Baumgarten and Kamrin (29) for this study, which has been successfully

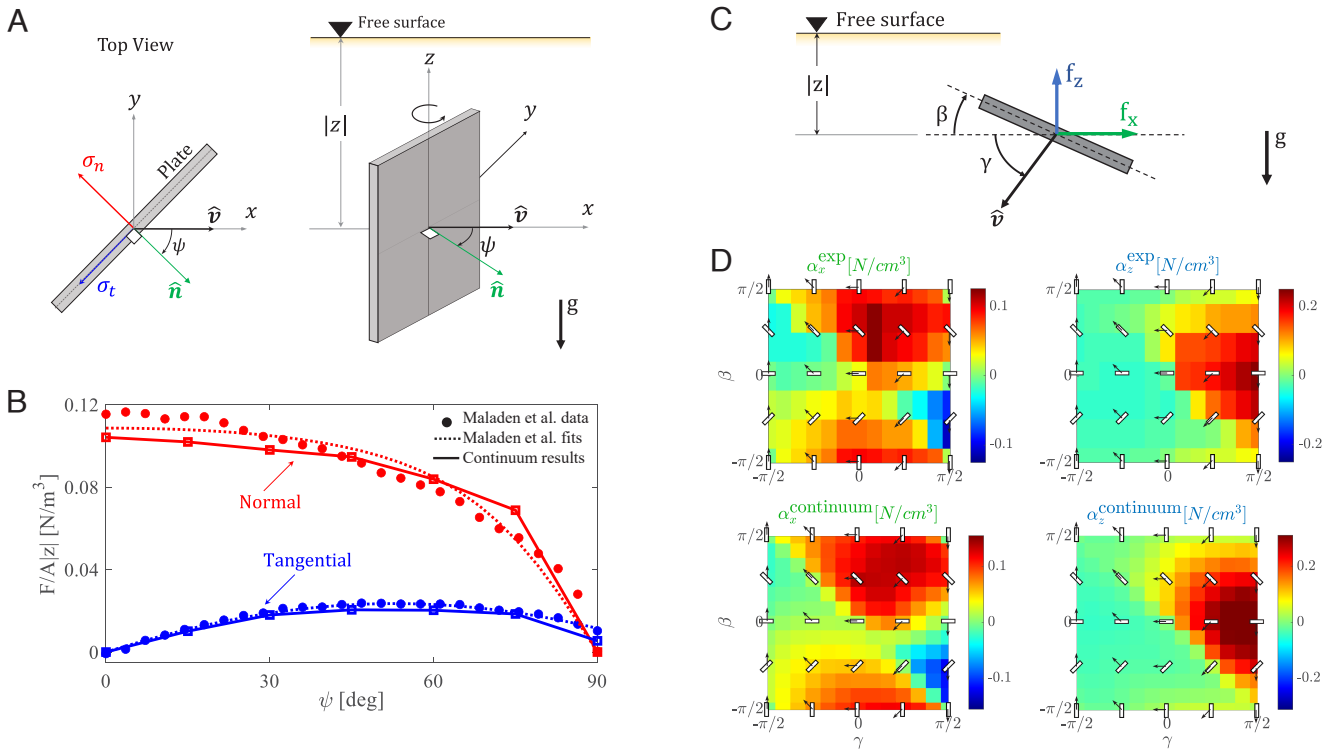

Fig. 7. Experiment vs. Continuum Model—Dependence on twist angle: (*A*) Schematic of plate orientations, and (*B*) Variations of normal (red) and tangential (blue) forces from Maladen et al. (48) experiments (• marker), their analytical fits to their results (dotted lines), and continuum simulations (■ marker with solid line). The forces are normalized by the plate center-depth ($|z|$) and plate area. Experiments (loosely packed 3-mm glass particles) as well as simulations use glass beads ($\rho_g = 2{,}500$ kg/m^3 and $\rho_c = 0.6$) as the granular media. Continuum simulations use $\mu_{\text{int}} = 0.4$ and $\mu_{\text{surf}} = 0.27$ in accordance with reported experimental values. Comparison of in-plane plate motions: (*C*) Schematic of plate orientation angle β and γ for in-plane motion study conducted using 3D simulation setup shown in Fig. 3 *A–D*. (*D*) Force/area/depth ($\boldsymbol{\alpha}$) from Li et al. (14) experiments (*Top*) and continuum simulations (*Bottom*). The plate configurations are also overlaid on graphs for clarity. The plates had no twist ($\psi = 0$) in regard to 3D-RFT definitions in these tests. Both the experiments and the simulations use glass beads with grain density (ρ_g) of 2,500 kg/m^3 and a packing fraction (ϕ_c) of 0.58. Internal friction is $\mu_{\text{int}} = 0.4$ and surface friction is $\mu_{\text{surf}} = 0.4$ for continuum simulations to match reported values in Li et al. (14).

used for modeling complex problems in the past (29, 30). For the continuum model to be useful to determine input data for a 3D-RFT, it must be shown to reliably match experiments for 3D plate intrusions. We test this in two scenarios.

In the first test case, we check whether the 3D-continuum simulations can regenerate the experimental variation of force/depth/area on flat plates in submerged granular beds from Li et al. (14). These experimental data were also used by Li et al. (14) in the generation of the 2D-RFT form. We use an effective material density of $\rho_c = 1{,}450$ kg/m^3 (loose glass beads, $\rho_g = 2{,}500$ kg/m^3, $\phi_c = 0.58$) in line with Li et al. (14) experiments and an approximate internal friction value for glass beads as $\mu_{\text{int}} = 0.4$. The media–plate surface friction was taken as $\mu_{\text{surf}} = 0.4$. The relative values of the forces from continuum results match the experimental observations quite well. The absolute values from continuum results, however, are higher than experiments by a constant multiplicative factor of $\sim$1.1. A smaller value of μ_{int} for glass beads could have provided a closer match to the experiments as the graphs are not expected to change their shape with changing internal friction values (14). But we do not attempt the exact calibration as the purpose of the test was to verify the accuracy of the continuum formulation and implementation. These results establish sufficient efficacy of the continuum model for plate motions in which the velocity, plate normal, and gravity are coplanar.

In the second test case, we assess the quantitative accuracy of the continuum approach in modeling in-plane as well as out-of-plane forces. We consider a study by Maladen et al. (48) which measured the normal and tangential forces on submerged plates moving horizontally in granular media as a function of plate twist (Fig. 7 *Top* for angles definition). The material properties are provided in the figure caption. The continuum results match observations from Maladen et al. (48) well.

The combination of the above two studies establishes the overall accuracy of the continuum model and its implementation for both in-plane and out-of-plane inputs and outputs in plate intrusion problems.

Data, Materials, and Software Availability. All study data are included in the article and/or *SI Appendix*.

ACKNOWLEDGMENTS. S.A. and K.K. acknowledge support from Army Research Office (ARO) grants W911NF1510196 and W911NF1810118, support from the US Army DEVCOM Ground Vehicle Systems Center, and NASA STTR Award Number 80NSSC20C0252. D.I.G. acknowledges support from ARO grant W911NF-18-1-0120. S.A. thanks Aaron Baumgarten, who provided the authors with his 3D-MPM model implementation. We also thank Andras Karsai for helpful discussions on potential forms of 3D-RFT. Portions of the paper were developed from the Ph.D. thesis of S.A.

1. S. T. Thoroddsen, A. Q. Shen, Granular jets. *Phys. Fluids* **13**, 4–6 (2001).
2. S. Agarwal *et al.*, Modeling of the interaction of rigid wheels with dry granular media. *J. Terramech.* **85**, 1–14 (2019).
3. P. E. Schiebel *et al.*, Mitigating memory effects during undulatory locomotion on hysteretic materials. *Elife* **9**, e51412 (2020).
4. N. Artemieva, B. Ivanov, Launch of Martian meteorites in oblique impacts. *Icarus* **171**, 84–101 (2004).
5. L. K. Treers, C. Cao, H. S. Stuart, Granular resistive force theory implementation for three-dimensional trajectories. *IEEE Rob. Autom. Lett.* **6**, 1887–1894 (2021).
6. A. J. Ijspeert, Biorobotics: Using robots to emulate and investigate agile locomotion. *Science* **346**, 196–203 (2014).
7. D. Van Der Meer, Impact on granular beds. *Ann. Rev. Fluid Mech.* **49**, 463–484 (2017).
8. R. He *et al.*, Review of terramechanics models and their applicability to real-time applications. *J. Terramech.* **81**, 3–22 (2019).

9. M. Bekker, Introduction to terrain-vehicle systems, 1969. *Ann. Arbor: Univ. Mich. Press* **1**.
10. J. Y. Wong, A. Reece, Prediction of rigid wheel performance based on the analysis of soil-wheel stresses part i. performance of driven rigid wheels. *J. Terramech.* **4**, 81–98 (1967).
11. H. B. Pacejka, E. Bakker, The magic formula tyre model. *Veh. Syst. Dyn.* **21**, 1–18 (1992).
12. J. Gray, G. Hancock, The propulsion of sea-urchin spermatozoa. *J. Exp. Biol.* **32**, 802–814 (1955).
13. C. J. Brokaw, Flagellar propulsion. *J. Exp. Biol.* **209**, 985–986 (2006).
14. C. Li, T. Zhang, D. I. Goldman, A terradynamics of legged locomotion on granular media. *Science* **339**, 1408–1412 (2013).
15. L. Huang, J. Zhu, Y. Yuan, Y. Yin, A dynamic resistive force model for designing mobile robot in granular media. *IEEE Rob. Autom. Lett.* **7**, 5357–5364 (2022).
16. R. D. Maladen, Y. Ding, C. Li, D. I. Goldman, Undulatory swimming in sand: Subsurface locomotion of the sandfish lizard. *Science* **325**, 314–318 (2009).
17. T. Zhang, D. I. Goldman, The effectiveness of resistive force theory in granular locomotion. *Phys. Fluids* **26**, 101308 (2014).
18. P. Jop, Y. Forterre, O. Pouliquen, A constitutive law for dense granular flows. *Nature* **441**, 727 (2006).
19. G. MiDi, On dense granular flows. *Eur. Phys. J. E* **14**, 341–365 (2004).
20. N. Gravish, P. B. Umbanhowar, D. I. Goldman, Force and flow at the onset of drag in plowed granular media. *Phys. Rev. E* **89** (2014).
21. H. Askari, K. Kamrin, Intrusion rheology in grains and other flowable materials. *Nat. Mat.* **15**, 1274–1279 (2016).
22. S. Dunatunga, K. Kamrin, Continuum modelling and simulation of granular flows through their many phases. *J. Fluid Mech.* **779**, 483–513 (2015).
23. S. Dunatunga, K. Kamrin, Continuum modeling of projectile impact and penetration in dry granular media. *J. Mech. Phys. Sol.* **100**, 45–60 (2017).
24. S. Agarwal, A. Karsai, D. I. Goldman, K. Kamrin, Efficacy of simple continuum models for diverse granular intrusions. *Soft Matter* **17**, 7196–7209 (2021).
25. S. Agarwal, A. Karsai, D. I. Goldman, K. Kamrin, Surprising simplicity in the modeling of dynamic granular intrusion. *Sci. Adv.* **7**, eabe0631 (2021).
26. S. Agarwal *et al*., Master's thesis (Massachusetts Institute of Technology) (2019).
27. J. Slonaker *et al*., General scaling relations for locomotion in granular media. *Phys. Rev. E* **95**, 052901 (2017).
28. Q. Zhang, S. Townsend, K. Kamrin, Expanded scaling relations for locomotion in sloped or cohesive granular beds. *Phys. Rev. Fluids* **5**, 114301 (2020).
29. A. S. Baumgarten, K. Kamrin, A general fluid-sediment mixture model and constitutive theory validated in many flow regimes. *J. Fluid Mech.* **861**, 721–764 (2019).
30. A. S. Baumgarten, K. Kamrin, A general constitutive model for dense, fine-particle suspensions validated in many geometries. *Proc. Natl. Acad. Sci. U.S.A.* **116**, 20828–20836 (2019).
31. F. Guillard, Y. Forterre, O. Pouliquen, Lift forces in granular media. *Phys. Fluids* **26**, 043301 (2014).
32. G. Smith, On isotropic functions of symmetric tensors, skew-symmetric tensors and vectors. *Int. J. Eng. Sci.* **9**, 899–916 (1971).
33. W. Kang, Y. Feng, C. Liu, R. Blumenfeld, Archimedes' law explains penetration of solids into granular media. *Nat. Commun.* **9**, 1–9 (2018).
34. G. Turk, M. Levoy, "Zippered polygon meshes from range images" in *Proceedings of the 21st Annual Conference on Computer Graphics and Interactive Techniques* (1994), pp. 311–318.
35. H. Suzuki, K. Katsushima, S. Ozaki, Study on applicability of RFT to traveling analysis of wheel with grousers: Comparison with DEM analysis as a virtual test. *J. Terramech.* **83**, 15–24 (2019).
36. S. Pravin *et al*., Effect of two parallel intruders on total work during granular penetrations. *Phys. Rev. E* **104**, 024902 (2021).
37. N. Gravish, P. B. Umbanhowar, D. I. Goldman, Force and flow transition in plowed granular media. *Phys. Rev. Lett.* **105**, 128301 (2010).
38. H. Katsuragi, D. J. Durian, Unified force law for granular impact cratering. *Nat. Phys.* **3**, 420 (2007).
39. A. A. Francoeur, K. M. Dorgan, Burrowing behavior in mud and sand of morphologically divergent polychaete species (annelida: Orbiniidae). *Biol. Bull.* **226**, 131–145 (2014).
40. S. Athani, P. Rognon, Pulling objects out of cohesive granular materials. *Granular Matter* **23**, 1–10 (2021).
41. A. Humeau, M. Piñeirua, J. Crassous, J. Casas, Locomotion of ants walking up slippery slopes of granular materials. *Int. Org. Biol.* **1**, obz020 (2019).
42. A. Soliman, S. Reid, W. Johnson, The effect of spherical projectile speed in ricochet off water and sand. *Int. J. Mech. Sci.* **18**, 279 (1976).
43. E. Wright *et al*., Ricochets on asteroids: Experimental study of low velocity grazing impacts into granular media. *Icarus* **351**, 113963 (2020).
44. H. C. Astley *et al*., Surprising simplicities and syntheses in limbless self-propulsion in sand. *J. Exp. Biol.* **223**, jeb103564 (2020).
45. C. Sunday *et al*., The influence of gravity on granular impacts-II. A gravity-scaled collision model for slow interactions. *Astron. Astrophys.* **658**, A118 (2022).
46. G. D. R. MiDi, On dense granular flows. *Eur. Phys. J. E* **14**, 341–365 (2004).
47. F. Da Cruz, S. Emam, M. Prochnow, J. N. Roux, F. Chevoir, Rheophysics of dense granular materials: Discrete simulation of plane shear flows. *Phys. Rev. E* **72**, 021309 (2005).
48. R. D. Maladen, Y. Ding, P. B. Umbanhowar, A. Kamor, D. I. Goldman, Mechanical models of sandfish locomotion reveal principles of high performance subsurface sand-swimming. *J. R. Soc. Interface* **8**, 1332–1345 (2011).
49. S. Agarwal *et al*., Ph.D. thesis (Massachusetts Institute of Technology) (2022).